BNL-65730

In situ Surface X-ray Scattering Studies of Electrosorption

J.X. Wang and R.R. Adžić

Chemical Sciences Division, Department of Applied Science

Brookhaven National Laboratory, Upton, NY 11973, USA

B. M. Ocko

Department of Physics

Brookhaven National Laboratory, Upton, NY 11973, USA

A short review of the application of surface x-ray scattering techniques to the electrode/electrolyte interfaces is presented. Recent results on metal, halide, and metal-halide adlayers with three specific systems, Bi on Au(100) and Au(110), Br on Au(100) and Ag(100), and the coadsorption of Tl with Br or I on Au(111), are given as an illustration. Factors affecting ordering of pure metal and halide adlayers and the metal-halide surface compounds are discussed in some detail.

I. INTRODUCTION

At electrode/solution interfaces, various metal and anion adlayers ranging from submonolayer to bilayer can be formed under thermodynamic equilibrium. For metal ions, this phenomenon, so-called underpotential deposition (UPD), occurs when the adatom-substrate bonding is stronger than the adatom-adatom bonding so that the first one or two monolayers are deposited at potentials positive of the Nernst potential for bulk deposition [1]. For anions, the monolayer is formed by chemisorption, usually called specific adsorption. This process occurs over a wide potential range below anion bulk oxidation or substrate dissolution potential, often involving partial charge transfer. At intermediate potentials, metal cations and anions can also coadsorb on electrode surfaces. These adlayers play an important role in interfacial electrochemistry since they profoundly affect the kinetics of many reactions [2]. The sensitivity of electrosorption to the substrate metal and crystallographic symmetry is known from electrochemical studies on single crystal electrodes. This has motivated structural studies using various methods to gain a microscopic understanding of electrode/electrolyte interfaces and to elucidate a wide variety of surface electrochemical processes.

A true atomistic picture of these adlayers on single crystal electrodes is emerging. This development has been accelerated by the introduction of *in situ* structural methods, specifically, scanning tunneling microscopy (STM), atomic force microscopy (AFM), and surface X-ray scattering (SXS). X-ray scattering has long been the most powerful technique for three-dimensional structure determination of solids. Its application to the study of two-dimensional structures at surfaces had been limited prior to the advent of intense synchrotron sources. In the past decade, SXS has become an increasingly important technique in surface science research [3,4]. Although most SXS studies to date have been carried out under UHV conditions, the penetrating nature of x-rays, unlike electron probes, allows studies to be carried out under well controlled electrochemical conditions. Since the first successful synchrotron SXS study of an underpotentially deposited metal monolayer a decade ago [5],

the technique has been applied to a wide variety of electrochemical phenomena including metal deposition, surface reconstruction, anion adsorption, surface oxide formation, surface water, and electrocatalysis. There are several reviews which describe the applications of *in situ* SXS techniques to interfacial electrochemistry [6,7].

In this article results from SXS studies of metal and halide adlayers on electrode surfaces are presented. For pure metal adlayers, we focus on the ordering of close-packed monolayers on various substrate surfaces, where the adatoms are significantly larger than the substrate atoms. On the close-packed (111) surfaces, Toney et al. have found that the underpotentially deposited Tl, Pb, and Bi adatoms form incommensurate structures similar to their vapor-deposited analogs [8]. Due to the inherently high spatial resolution of SXS the incommensurate structures can be measured with high precision, thus permitting small potential dependent changes in lattice spacing of the monolayer to be determined. From such data the monolayer compressibility is calculated. In section III, studies of UPD on more open surfaces, (100) and (110), are presented, along with a discussion of the factors that affect the ordering, symmetry, and the density of metal monolayers. In section IV, studies of potential induced second order phase transitions for Br adlayer are presented and the results are compared with universal phase transition theories. In section V, results from Tl coadsorption with halides are presented and these illustrate the effect of partial charge on the structure and the stoichiometry of coadsorbed adlayers. The quantitative results obtained from *in situ* SXS are complementary to those obtained with real space scanning probes.

II. EXPERIMENTAL

A determination of surface structures with SXS involves measurements of the distribution of scattered x-rays in reciprocal space, (H,K,L), and a comparison of the diffraction pattern and intensity distribution with atomic models. To illustrate the relationship between real and reciprocal space, a (2×2) adlayer on a rectangular substrate is shown in Fig. 1. In reciprocal space (Fig. 1b), the diffraction is a two-dimensional (2D) lattice of rods. Each rod is a line of scattering which is sharp in both directions parallel to the surface (H and K) and

diffuse along the surface normal direction (L). The solid lines show the crystal truncation rods (CTR) which pass through the Bragg points of the bulk [9]. In addition, surface rods (dashed lines) arise at half order positions from the (2×2) adlayer. Typical rod profiles are shown in Fig. 1d. While the intensity of a surface rod monotonically decreases, the CTR intensity rises sharply near the Bragg points where many layers contribute to the scattering.

Information pertaining solely to the structure within the surface plane is obtained with a grazing incidence angle (typically 1.2°), where L is small. From the in-plane diffraction pattern (Fig. 1c) where the observed peaks are described by the two component vector (H, K), the superlattice structure is deduced. On the other hand, when the scattering vector is aligned entirely along the surface normal direction (e.g., no in-plane component) the electron density profile normal to the surface is obtained, independent of the specifics of the in-plane ordering. This geometry is referred to as specular reflectivity since the angle between the surface plane and incident wave vector is equal to the angle between the surface plane and the scattered wave vector [7,10]. Additional structural information is obtained from the intensity distribution along the surface normal direction at a fixed (H, K) positions corresponding to either the bulk crystal structure (i.e., the CTR) or to the surface structure (i.e., the surface rod) [4].

A thin layer x-ray scattering electrochemical cell, see Fig. 1, is usually used in SXS studies of electrode surfaces. In our measurements, a 4-μm thick plastic x-ray window seals the cell which makes a thin, 10$\sim$20 μm, solution layer between the crystal face and the film. An outer chamber was filled with high purity nitrogen gas to prevent oxygen diffusing through the thin film during the measurements. Compared with UHV measurements, the presence of electrolyte and the plastic film significantly increases the background signal and limits the ability to detect weak peaks. Despite this limitation, diffraction from monolayers of low-Z atoms, such as Cl, has been observed [11]. A reversible hydrogen electrode (RHE) was used in acid solution, especially for halide-free solutions and a Ag/AgCl(3M NaCl) reference electrode was used for halide-containing solutions.

The data reported here were obtained with focused, monochromatic synchrotron radia-

tion at beam lines X22A ($\lambda \sim 1.20$ Å) and X22B ($\lambda \sim 1.54$ Å) at the National Synchrotron Light Source (NSLS). In the four circle geometry, the sample was oriented through its Euler angles θ, χ, and ϕ by a spectrometer under computer control [12]. The magnitude of the scattering wave vector is $\left|\vec{k_f} - \vec{k_i}\right| = (4\pi/\lambda)sin(2\theta/2)$, where $\vec{k_i}$ and $\vec{k_f}$ correspond respectively to the incident and scattered wave vectors and 2θ is the angle between these two vectors. Diffraction measurements were carried out by measuring the scattering intensity along paths in reciprocal space in the "$\omega = 0$ geometry" [13]. Soller slits or a LiF(200) analyzer crystal were used for achieving a high radial in-plane resolution and for reducing the diffuse x-ray scattering background from the film and electrolyte. The integrated intensities, however, were measured with regular slits located 600 mm from the sample, typically 2 mm within the scattering plane. This ensures that the in-plane radial peak widths were larger than the intrinsic peak widths. The structure factors were obtained after correcting the integrated intensities for the variation of the Lorentz factor, the effective sample area, and the resolution along the surface normal direction [14].

III. METAL DEPOSITION: Bi ON Au(100) AND Au(110)

The UPD processes often exhibit features in voltammetry curves sensitive to the crystallographic structures of the electrode. Hence, it has been speculated that these metal adlayers form ordered structures on single crystal electrodes. Indeed, well ordered superlattice structures have been observed by using SXS for many UPD metals (Tl,Pb,Bi,Ag,Hg) on the least corrugated (111) surfaces (Ag,Au,Pt,Cu) [5,8,15–23] and for Tl on the more corrugated (100) surfaces (Au,Ag) [24,25]. Here, we present recent SXS studies of the UPD of Bi on Au(100) and Au(110) and discuss the structure-determining factors for fully discharged UPD metal monolayers.

Fig. 3 shows the voltammetry curves for the UPD of Bi on the (111), (100), and (110) surfaces of gold in 0.1 M $HClO_4$ solution. The major deposition peaks shift to more positive potentials on the (100) and (110) surfaces as compared to those on the (111) surface. This is consistent with theoretical calculations which show that chemisorbed adatoms prefer the

highest coordination (hollow) sites and the bonding energy increases as the surface becomes more open [26]. The deposition of a close-packed Bi monolayer at potentials prior to the onset of bulk deposition can be ascertained from the integrated charges for all three surfaces. Currents between 0.7 V and the low potential limits were integrated for both the cathodic and anodic sweeps. Averaging the integrals from both sweeps gives 445, 472, and 357 $\mu C/cm^2$ for Au(111), Au(100), and Au(110), respectively. Assuming Bi^{3+} is fully reduced, the charge required for depositing one Bi atom per surface gold atom is 666, 576, and 408 $\mu C/cm^2$ for the (111), (100), and (110) surfaces, respectively. On Au(111), the Bi coverage is 445/666 = 0.67 monolayer, which is close to the coverage (0.646) obtained from SXS measurements at the most negative potential [17]. The atomic density of the uniaxially commensurate Bi monolayer (see the model in Fig. 3) is 6% higher than that in the bulk environment (see Fig. 5 caption for the definition). Since the charges measured by voltammetry for the (100) and (110) surfaces are similar to that for the (111) surface, the Bi monolayers on Au(100) and Au(110) are expected to be close-packed. SXS measurements were carried out for the Au(100) and Au(110) surfaces to investigate the influence of the substrate lattice on these Bi monolayers.

In Fig. 4, the diffraction patterns obtained for the UPD of Bi on Au(100) and Au(110) are shown with the corresponding real space models. For Au(100), only one of the two symmetry-equivalent domains is shown. The adlayer diffraction pattern (circles) has the characteristics of a *centered* rectangular lattice, i.e., the diffraction intensity is zero at $(m/p,n/2)$ when the sum of m and n is odd. Here, p is non-integral and thus the unit cell is uniaxially incommensurate. This monolayer exists within 40 mV positive of the onset of bulk deposition. The Bi diffraction peaks shift slightly with potential along the incommensurate direction, hence, the adlayer lattice is uniaxially electrocompressible. The coverage calculated from the lattice constants ranges from 0.798 to 0.776 relative to the atomic density of Au(100) surface. The coverage calculated from the charge is 473/576 = 0.82, in reasonable agreement with the SXS results.

On Au(110) the non-integer diffraction peaks are found at $(1/p,0)$, $(1/p,1)$, and $(2/p,0)$

positions, as shown in Fig. 4 (bottom, left), where p changes from 1.148 to 1.142 over a 0.15 V potential range. The corresponding coverages ($\theta = 1/p$, where θ varies from 0.871 to 0.876) are also consistent with that calculated from the charge (357/408=0.875). Since the surface is free of Bi at potentials positive of 0.7 V, the decrease in the (0,1) peak intensity with the deposition of Bi indicates that the Bi adatoms diffract out-of-phase with those from the Au substrate, and must be centered with respect to substrate unit cell along the y-axis. The (1,0) peak intensity changes less over the same potential range, reflecting the fact that the Bi adatoms do not have fixed positions along the x-axis, where the adlayer is incommensurate with the substrate.

On the Au(110) and Au(100) surfaces, the substrate unit cell has the same 2.885 Å spacings along the x-axis. If the lattice mismatch along the incommensurate direction was not important, then Bi would form the same c($2 \times p$) phase on Au(110) as on the Au(100) surface, albeit with a different value of p. This is not the case. Rather, a ($p \times 1$) structure, with the commensuration along the more corrugated y-axis, is formed. For this structure, the uneven near neighbor spaings are unusually large (22% larger along the y axis than that along the x axis), which is unfavorable for most of close-packed monolayers. For example, thallium, which also forms a c($p \times 2$) monolayer on Au(100) [24], forms no ordered monolayer on Au(110). The lack of the ($p \times 1$) Tl phase is likely due to the more metallic character of Tl than Bi, and hence a stronger tendency towards even lateral bondings in a hexagonal symmetry. This is supported by the difference in the bulk crystal structures (hcp versus rhl) [27] and the monolayer structures on the Ag and Au (111) surfaces (rotated-hexagonal for Tl [15,19] and uniaxially-centered-rectangular for Bi [16,17]).

In general, when the size of an adatom is significantly larger than the substrate lattice site, an ordered adlayer has to be incommensurate at full coverage. From SXS studies of the UPD of Tl, Pb, and Bi [5,15–19,8,20,22,24,25,28], 2D incommensurate structures have been observed on the (111) surfaces of several metals, but not on any of more open and corrugated (100) and (110) surfaces. On these surfaces, ordered adlayers are found to be commensurate with the substrate along at least one direction, where the adatoms are situated between the

rows, thus avoiding unfavorable atop sites.

The layer densities for the close-packed monolayer structures of Tl, Pb, and Bi formed on the three low index gold surfaces as a function of potential are summarized in Fig. 5. These densities have been normalized to those of their bulk phase. On the least corrugated Au(111) surface (circles), all three adatoms (Tl, Pb, and Bi) form an ordered monolayer with a potential dependent layer density ranging from near unity to 1.06, where the adatom-adatom interaction dominates. On Au(100), both Tl and Bi form a $c(p \times 2)$ uniaxially incommensurate structure, while Pb appears to form commensurate $c(2 \times 2)$ adlayer with small patches of anti-domain phases [28], i.e., only orders in short range. As the substrate corrugation and lattice mismatch increases on the (110) surface, Bi is the only one which forms ordered close-packed monolayer. The higher (up to 6%) layer densities are often observed for incommensurate metal monolayers since the reduced coordination at a surface enhances lateral bonding with neighbors which favors higher surface densities. An incommensurate metal monolayer with more than 10% compression or expansion relative to bulk is often highly strained, and thus is rare. The ordered phase observed for Bi monolayer on Au(100) (10% compressed) and Au(110) (12% expanded) likely result from the covalent bonding characteristics of Bi.

Besides the lattice geometry effects discussed above, the specifics of the substrate-adatom interaction also influence the structure of UPD metal adlayers. For example, Tl forms a well ordered bilayer prior to bulk deposition on both Ag(111) [15] and Ag(100) [25], but not on the Au and Pt electrodes. Platinum, as a transition metal, shows distinct effects: a high order commensurate Pb monolayer [18] and an aligned hexagonal Tl monolayer [20] are formed on Pt(111) in contrast to the incommensurate rotated-hexagonal monolayers of Pb and Tl on the Ag(111) and Au(111) surfaces.

IV. HALIDE MONOLAYERS: BROMIDE ON Au(100) AND Ag(100)

Halides (Cl, Br, and I), similar to the UPD metals discussed in the previous section, also form well ordered monolayer phases below its bulk oxidation or substrate dissolution poten-

tial. Synchrotron x-ray scattering studies have shown that the structure of these phases may be commensurate or incommensurate with the underlying noble metal electrodes [11,29–36]. On the Au(111) surface, for instance, halide ions (Cl, Br, and I) form incommensurate hexagonal monolayers which compress with increasing potentials [11,30,29]. In the case of bromide, the nearest neighbor separation decreases from 4.24 to 4.03 Å as the potential is increased over a 0.3 V range. Over the entire potential range the adsorbed bromide monolayer remains incommensurate.

As for many other adsorbates, the symmetry of the underlying electrode affects the epitaxy of adsorbed halides. On the square Au(100) surface, a commensurate $c(\sqrt{2} \times 2\sqrt{2})R45°$ Br monolayer is formed at intermediate potentials (See Fig. 6, top/left), which becomes uniaxially incommensurate and electrocompressible at the most positive potentials. The distortion from hexagonal symmetry is reduced by the uniaxial lattice compression and the maximum coverage is similar to those found on Au(111), showing a moderate effect of substrate symmetry. On Ag(100), however, a square $c(2 \times 2)$ Br adlayer is formed where the Br adatoms are adsorbed in the fourfold hollow sites (see Fig. 6 top/right). Since Ag has nearly the same lattice constants as Au, this demonstrates that the stronger chemical affinity between halide and silver enhances the site specific adsorption. The bromide adlayers on both Au(100) and Ag(100) have the same 1/2 monolayer coverage despite their different symmetries. The in-plane diffraction patterns observed from these two adlayers are shown in the bottom of Fig. 6. Besides the half-order peaks, e.g., (1/2,1/2) and (3/2,1/2), quarter-order peaks, such as (1/4,3/4) and (1/4,5/4) peaks were observed from Br on the Au(100) surface. This diffraction pattern results from two symmetry equivalent domains, where the long lattice constant lies along, or vertical to, the (1,1) substrate axis. As the phase becomes incommensurate at high potentials, the peaks shift along the (1,1) or (-1,1) directions accordingly. Both systems exhibit simple second order phase transition, an Ising like order-disorder transition on the Ag(100) surface [35] and an 1D commensurate-incommensurate transition on the Au(100) surface [32].

For bromide adsorption on the Au(100) surface the potentials where new diffraction

features appear are well correlated with the peaks in the cyclic voltammogram shown in Fig. 7. At potentials below P1, all of the diffraction features are associated with the square pattern from the underlying gold substrate. Positive of P1, additional reflections appear, which correspond to a rectangular, commensurate $c(\sqrt{2} \times 2\sqrt{2})R45°$ unit cell, as shown in the top/left of Fig. 6 and in the insert of Fig. 8. Further analysis of the diffraction reveals that the adsorbed bromides are positioned on the bridge sites [32]. Over the entire potential range between P1 and P2 there is no change in the symmetry or in the coverage of bromides.

At potentials above P2 (ca. 0.42 V) the bromide monolayer is compressed uniaxially as shown in Fig. 8, where $p < 2\sqrt{2}$. The incommensurability, ϵ, is related to the inverse of p. In the commensurate $c(\sqrt{2}\times 2\sqrt{2})R45°$ phase ϵ=0. In the incommensurate $c(\sqrt{2}\times p)R45°$ phase ϵ varies continuously from 0 to 0.13, as shown in Fig. 8. The phase transition is nearly reversible and appears to be second order. The uniaxial compression reduces the symmetry distortion of the quasi-hexagonal lattice, and when $\epsilon = 0.13$, the lattice is nearly perfectly hexagonal. At the maximum coverage, the nearest neighbor separations are close to the value expected on the basis of the Van der Waals radius and to the measured value for bromide on Au(111).

Pokrofsky and Talapov have predicted that an incommensurate phase forms from the commensurate phase when entropically wandering, non-interacting domain walls appear [38]. They predict that the incommensurability should follow a power-law with the reduced chemical potential with a critical exponent $\beta = 1/2$. The best fit to a power-law form to the incommensurability, as shown by the solid line Fig. 8, gives a critical exponent $\beta = 0.4$; statistically smaller than the Pokrofsky and Talapov prediction. In addition, their model predicts sharp domain walls rather than a uniform compression. The absence of satellite peaks for Br on Au(100), within the limits of the diffuse scattering background, establishes that the compression is nearly uniform and not a network of locally commensurate regions separated by domain walls [32].

We now turn our attention to the electrodeposition of bromide on the Ag(100) surface. Here the surface exhibits an order-disorder phase transition at a critical potential which

corresponds to a transformation between a "lattice gas" phase, with short range positional order and a commensurate phase, with long range positional order. The order-disorder transition is predicted to be second order and is isomorphic to the two dimensional Ising model in magnetism [37]. The analogy to the Ising model requires the adsorbate atoms to reside at lattice sites and the near-neighbor lateral interactions to be repulsive. According to the Ising model, the order-disorder transition occurs at a critical coverage of 0.368 and the order parameter should follow a power-law with a critical exponent of 1/8 [39,40].

On the Ag(100) surface, under vacuum [39] and electrochemical conditions [35], an ordered $c(2\times2)$ structure is observed above a critical coverage where the halides are situated in the fourfold hollow sites of the underlying silver lattice. Although both the $c(2\times2)$ and the $c(\sqrt{2}\times2\sqrt{2})R45°$ structures have the same half monolayer coverage, the packing arrangement on Ag(100) is square compared to the quasi-hexagonal structure found on Au(100). Measurements of the scattered intensity at the (1/2,1/2) position versus the applied potential from the Ag(100) surface in 0.05 M NaBr (see Fig. 9) reveal a phase transition at -0.76 V associated with the development of long-range order of the adsorbate. The intensity is zero below this potential and increases sharply at the potential corresponding to a cusp like current peak in the cyclic voltammogram shown in Fig. 9.

In a SXS measurement, the registry of an ordered adlayer or the adsorption sites in a disordered phase can be inferred from analysis of the crystal truncation rods. By considering the scattering amplitude from the semi-infinite sum over the Ag(100) lattice, both with and without a half monolayer of bromide atoms at the fourfold hollow sites, it can be shown that the scattered x-ray intensity at (0,1) is expected to be 11% of the value obtained in the absence of bromide. The intensity indeed decreases to 11% of its level with no bromide, as shown in the middle panel of Fig. 9, when the potential increases from -1.0 V (no adsorbed bromide) to -0.3 V and supports the adsorption of a half a monolayer in the fourfold symmetry sites. Exchanging the bromide ions with chloride ions does not change the halide adsorbate structure. The interference effects, however, are reduced since there are significantly fewer electrons for a chloride atom compared to the number in a bromide

atom. With chloride the intensity falls to 44%, also in agreement with the simple interference calculation described above [35]. The decrease of the (0,1) scattering intensity, at potentials more negative of the ordered phase, is consistent with the interference expected for lattice gas adsorption at the fourfold hollow sites.

These results clearly indicate that electrodeposited bromide on Ag(100) undergoes an order-disorder transition. Comparison with the Ising model confirms the essential predictions of the model. The top panel of Fig. 9 shows reasonable agreement between the data (circles) and fitted model curve (solid line) obtained by using the power-law form with a fixed Ising model critical exponent of 1/8. In addition, the critical coverage of 0.35 where the order-disorder transition occurs at -0.76 V is in agreement with the Ising model prediction of 0.368.

V. METAL-HALIDE COADSORPTION: Tl-Br AND Tl-I ON Au(111)

The UPD of metals is known to be dependent on the specific adsorption of anions. Unlike the systems described in section III, which do not involve specifically adsorbed anions, strongly adsorbed anions can cause formation of coadsorbed metal-anion phases. For the UPD of Cu in the presence of sulfate, chloride, and bromide on Au and Pt surfaces [42–46], a bilayer forms with Cu directly contacting the substrate and the anion in the second adlayer. The anion adsorption is enhanced due to a stronger interaction of the anions with the partially charged Cu adatoms than with the Au or Pt substrate. This, in turn, stablizes the low-coverage Cu adlayers. An illuminating counter example, with opposite anion/cation distribution in the adlayer is provided when alkali-metal cations coadsorb with iodide on Au(110) [47]. In this system, the anion interaction with the substrate is much stronger than that of the metal cation, causing the formation of coadsorbed adlayer with the anion chemisorbed on the substrate and the cation being coadsorbed.

In this section we present results for the coadsorption of Tl with Br or I on Au(111). Here the cation-substrate, anion-substrate, as well as cation-anion (in adsorbed phase) interactions are comparable in strength over a wide potential region. A more complex phase

behavior is seen and the structures of coadsorbed adlayers can be best understood in terms of the formation of surface compounds, where the partial charge on the adions plays an important role in determining the stoichiometry and the lattice symetry [48,49].

For thallium-bromide electrosorption on the Au(111) surface three mixed and two pure adlayer phases are formed at different potentials. The voltammetry curve (see Fig. 10) shows a multitude of reversible peaks over a wide potential region. The peaks labeled by the letters are associated with the phase transitions. Real space atomic models, corresponding to the five ordered phases determined from x-ray diffraction measurements, are shown in the potential range where they occur. The hexagonal bromide adlayer disorders at about 0.9 V where thallium starts to coadsorb. As the potential is further decreased over a 0.7 V potential region, two well-ordered commensurate and one weakly-ordered incommensurate phases appear. At the most negative potentials a rotated-hexagonal Tl monolayer forms.

The structure factor analysis for the commensurate phases shows the formation of $TlBr_2$ and TlBr surface compounds in the 3-$(\sqrt{13} \times \sqrt{13})$ and 2-$(3 \times \sqrt{3})$ phases, respectively. For the 2TlBr-$(3 \times \sqrt{3})$ structure the bromide ions are situated at the gold bridge sites and thallium ions are situated near the hollow sites. In addition, the top layer of Au atoms is displaced laterally along the $\sqrt{3}$ direction. This results in a more even separation between Tl and the three neighboring Au atoms and an increase of the Br-Au separation. A discussion on gold surface relaxation is published elsewhere [49].

The lower panel shows the potential dependent diffraction intensities for the three mixed phases at the corresponding reciprocal space positions. These scans identify the potential intervals of the observed phases and coexistence between two different phases characteristic of first order phase transitions. The bromide and thallium coverages are respectively shown by the open and closed circles.

The electrosorption reactions leading to the formation of these phases involve a partial charge transfer. The positive charge on metal adsorbates increases and the negative charge on adsorbed bromide decreases with increasing potential. This leads to a phase transition involving a change of stoichiometry from TlBr to $TlBr_2$ and a lattice symmetry change from

quasi-square to hexagonal.

Similar phase behavior has been observed for the coadsorption of Tl with I on Au(111). Since iodide is larger than bromide, the centered-rectangular phase for TlI is 3TlI-$(5 \times \sqrt{3})$, which has a slightly lower coverage (0.3 monolayer) than that of TlBr (0.333 monolayer). At higher potential, a TlI_3-(3×3) hexagonal phase has been observed. Relative to $TlBr_2$, the higher anion to cation ratio occurs since iodide is more discharged than bromide. An analysis of the hexagonal phase x-ray data is presented below.

Fig. 11 shows models of the 3$TlBr_2$-$(\sqrt{13} \times \sqrt{13})$ and TlI_3-(3×3) structures, both hexagonal, with their corresponding in-plane diffraction patterns. While the lattice constants and the azimuthal orientations are determined from the observed in-plane peak positions, the ratio and arrangement of the two species within the unit cell are deduced from the intensity analysis. The intensities have been measured at grazing incidence geometry ($L = 0.2$) by integrating the θ rocking curves of each surface diffraction peak in the (H, K) plane. The results, after correcting for the variation of the Lorentz factor, the effective sample area, and the resolution along the surface normal direction [14], are shown by the areas of the open circles in Fig. 11c and 11d.

For $TlBr_2$ the primitive unit cell with one Tl ion at the origin and two Br ions at the two triangular sites, depicted by the solid line in Fig. 11a, was used for the calculation of structure factor intensity. As shown in Fig. 9c, the calculated intensities, represented by the size of the "+" sign, are consistent with those measured (circles). If only one Br per Tl is assumed, the calculated intensity for the first order peak is at least 50% higher than the measured value. Since this is far above the experimental uncertainty, the TlBr model can be ruled out.

For the (3×3) phase (see Fig. 11b) two high symmetry models, TlI_3 and Tl_3I, yield nearly identical intensity distribution pattern, though the absolute intensities are somewhat higher for Tl_3I due to the higher Z of Tl than I. Since the measured intensities cannot be easily converted to absolute values, the data are normalized so that the strongest peak has the same value as that calculated. Therefore, the agreement (see Fig. 11d) between the

data (size of the circles) and calculated values (size of the "+" signs) supports both models.

In order to distinguish the two models and to determine the adlayer spacing from the substrate surface, specular reflectivity measurements were carried out for the (3×3) phase. Fig. 12 shows the integrated intensities at different L along the (0,0,L) rod, where the normalization factor is obtained by fitting the data near the (0,0,3) Bragg position. The data (circles) clearly differ from the adsorbate-free Au(111) reflectivity profile (dotted line) and are analyzed using a real space density model which incorporates an ideally terminated Au(111) crystal, a non-ideal Au top layer, a thallium, and an iodide monolayer. Each of these three surface layers is described by an atomic coverage normalized to an ideal Au(111) plane, a layer spacing, a vertical root-mean-square (rms) displacement amplitude, and a species-dependent atomic form factor. While the density of the Au top layer is always fixed at unity, the Tl coverage is held at either 0.11 or 0.33 with the I coverage fixed at 0.33 or 0.11, respectively. The former corresponds to the TlI_3 model and gives a much better fit (solid line) than the latter that represents the Tl_3I model (dashed line). For the TlI_3 model, the layer spacing between the Au top layer and the I and Tl adlayers are 2.6 and 3.5 Å, respectively. In contrast, bromide ions in the $TlBr_2$-$(\sqrt{13} \times \sqrt{13})$ phase are found, from analysis of specular reflectivity profile (not shown), to be in two layers more than 3 Å apart [49]. These results can be understood by comparing the adsorbate sizes with the lattice spacings. For $TlBr_2$ (see Fig. 11a) the nearest neighbor separation (3.47 Å), calculated from a 2D lattice, is much smaller than the diameter of bromide (3.92 Å [27]). In the TlI_3 adlayer, on the other hand, the iodide ion (4.3 Å in diameter [27]) is slightly smaller than the in-plane nearest neighbor separation (4.32 Å) (see Fig. 11b).

The results discussed above demonstrate that well ordered surface compounds can be formed by coadsorption of cations and anions. The stoichiometry and the lattice structure of these compounds are influenced by the substrate and applied potential. Further studies of various metal-anion surface compounds will enhance our understanding of 2D ionic crystals.

VI. CONCLUSIONS

Recent SXS studies of metal (Tl, Pb, and Bi), halide (Cl, Br, and I), and metal-halide coadsorbed adlayers are discussed with examples chosen to highlight the strength of *in situ* SXS techniques viz., (1) high accuracy for determining the density and compressibility of incommensurate adlayers; (2) quantitative measure of potential induced structural phase transitions; (3) reliable structural determination of mixed adlayer from analysis of the scattering intensity. From these results, a better connection between surface science and electrochemistry is established. The similarity in structures and phase behavior for pure metal and halide adlayers deposited in vacuum and in electrochemical cell shows that the structure-determining interactions are similar in both cases for most systems. Therefore, the electrochemical adsorption of pure elements can be well understood with established theories and concepts in surface science. On the other hand, electrochemistry provides unique opportunities for obtaining accurate information near the critical point in structural phase transitions and for studying a variety of ionic surface compounds.

Acknowledgements

This work was supported by the US Department of Energy, Divisions of Chemical and Materials Sciences, under Contract No. DE-AC02-98CH10886. We have benefitted from collaboration and discussions with Olaf Magnussen, Thomas Wandlowski, Ian Robinson, and Steve Feldberg.

REFERENCES

[1] DM Kolb. In: H Gerischer, CW Tobias, eds. Advances in Electrochemistry and Electrochemical Engineering. Vol. 11. New York: Wiley-Interscience, 1978, pp 125-271.

[2] RR Adžić. In: H Gerischer, CW Tobias, eds. Advances in Electrochemistry and Electrochemical Engineering. Vol. 13. New York: Wiley-Interscience, 1984, pp 159-260.

[3] R Feidenhans'l. Surf. Sci. Rep. 10:105-188, 1989.

[4] IK Robinson, DJ Tweet. Rep. Prog. Phys. 55:599-651, 1992.

[5] (a) MG Samant, MF Toney, GL Borges, L Blum, OR Melroy. Surf. Sci. 193:L29-L36, 1988. (b) MG Samant, MF Toney, GL Borges, L Blum, OR Melroy. J. Phys. Chem. 92:220-225, 1988.

[6] (a) MF Toney, JG Gordon, OR Melroy. SPIE Proc. 1550:140, 1991. (b) MF Toney, OR Melroy. In: HD Abruna, ed. Electrochemical Interfaces: Modern Techniques for In-Situ Interface Characterization. Berlin: VCH Verlag Chemical, 1991, pp 57-129. (c) MF Toney. In: CA Melendres, A Tadjeddine, eds. Synchrotron Techniques in Interfacial Electrochemistry. Dordrecht: Klewer, 1994, pp 109-125. (d) BM Ocko, J Wang. In: CA Melendres, A Tadjeddine, eds. Synchrotron Techniques in Interfacial Electrochemistry. Dordrecht: Klewer, 1994, pp 127.

[7] BM Ocko, OM Magnussen, JX Wang, RR Adžić. In: AA Gewirth, H Siegenthaler, eds. Nanoscale Probes of the Solid/Liquid Interface. Netherlands: Kluwer Academic Publishers, 1995, pp 103-119.

[8] MF Toney, JG Gordon, MG Samant, GL Borges, OR Melroy, D Yee, LB Sorensen. J. Phys. Chem. 99:4733, 1995.

[9] IK Robinson. Phys. Rev. B 33:3830, 1986.

[10] D Gibbs, BM Ocko, DM Zehner, SGJ Mochrie. Phys. Rev. B 38:7303, 1988. D Gibbs,

BM Ocko, DM Zehner, SGJ Mochrie. Phys. Rev. B 42:7330, 1990. BM Ocko, D Gibbs, KG Huang, DM Zehner, SGJ Mochrie, Phys. Rev. B 44:6429, 1991. AR Sandy, SGJ Mochrie, DM Zehner, KG Huang, D Gibbs. Phys. Rev. B 43:4667, 1991.

[11] OM Magnussen, BM Ocko, RR Adžić, JX Wang. Phys. Rev. B 51:5510, 1995.

[12] WR Busing, HA Levy. Acta Cryst. 22;457, 1967.

[13] SGJ Mochrie. J. Appl. Cryst. 21:1, 1988.

[14] IK Robinson. In: DE Moncton, GS Brown. eds. Handbook on Synchrotron Radiation. Vol. 3. Amsterdam: North-Holland, 1991, pp 221.

[15] (a) MF Toney, JG Gordon, MG Samant, GL Borges, OR Melroy, D Yee, LB Sorensen. Phys. Rev. B 45:9362, 1992. (b) MF Toney, JG Gordon, MG Samant, GL Borges, OR Melroy, LS Kau, DG Wiesler, D Yee, LB Sorensen. Phys. Rev. B. 42:5594, 1990.

[16] MF Toney, JG Gordon, MG Samant, GL Borges, DG Wiesler, D Yee, LB Sorensen. Langmuir 7:796, 1991.

[17] CH Chen, KD Keple, AA Gewirth, BM Ocko, JX Wang. J. Phys. Chem. 97:7290, 1993.

[18] RR Adžić, JX Wang, CM Vitus, BM Ocko. Surf. Sci. 293:L876, 1993.

[19] JX Wang, RR Adžić, BM Ocko. J. Phys. Chem. 98:7182, 1994.

[20] RR Adžić, JX Wang, OM Magnussen, BM Ocko. J. Phys. Chem. 100:14721, 1996.

[21] J Li, HD Abruna. J. Phys. Chem. B 101:2907-2916, 1997.

[22] YS Chu, IK Robinson, AA Gewirth. Phys. Rev. B 55:7945-7954, 1997.

[23] JX Wang, NS Marinkovic, RR Adžić, BM Ocko. Surf. Sci. 398:L291-296, 1998.

[24] JX Wang, RR Adžić, OM Magnussen, BM Ocko. Surf. Sci. 335:120-128, 1995.

[25] JX Wang, RR Adžić, OM Magnussen, BM Ocko. Surf. Sci. 344:111-121, 1995.

[26] MI Rojas, SA Dassie, EPM Leiva. Zeits. Phys. Chem. Bd. 185:33-50, 1994. E Shustorovich. Surf. Sci. rep. 6:1-63, 1986. E Shustorovich. Adv. Catal. 37:101-163, 1990.

[27] J Emsley. The Elements. 2nd ed. Oxford: Clarendon Press, 1991.

[28] KM Robinson, WE O'Grady. In: CA Melendres, A Tadjeddine. eds. Synchrotron Techniques in Interfacial Electrochemistry. Vol. 432, Boston: Kluwer Academic Publishers, 1994, pp 157-169.

[29] BM Ocko, GM Watson, J Wang. J. Phys. Chem. 98:897, 1994.

[30] OM Magnussen, BM Ocko, JX Wang, RR Adžić. J. Phys. Chem. 100:5500, 1996.

[31] BM Ocko, OM Magussen, JX Wang, RR Adžić, T. Wandlowski. Physica B 221:238, 1996.

[32] BM Ocko, OM Magussen, JX Wang, T. Wandlowski. Phys. Rev. B53:R7654, 1996.

[33] T Wandlowski, JX Wang, BM Ocko, OM Magussen. J. Phys. Chem. 100:10277, 1996.

[34] CA Lucas, NM Markovic, PN Ross. Phys. Rev. B 55:7964-7971, 1997.

[35] BM Ocko, JX Wang, T. Wandlowski. Phys. Rev. Lett. 79:1511, 1997.

[36] JX Wang, T Wandlowski, BM Ocko. In: C Koreniewski, BE Conway. eds. Proceedings of the Symposium on the Electrochemical Double Layer. Vol. 97-17, The Electrochemical Society, Inc., 1997, pp293-301.

[37] BNJ Person. Surf. Sci. Rep. 15:1, 1992.

[38] VL Pokrofsky, AL Talapov. Phys. Rev. Lett. 42:66, 1979.

[39] DE Taylor, ED Williams, RL Park, NC Bartelt, TL Einstein. Phys. Rev. B 32:4653, 1985.

[40] JP van der Eerden, G Staikov, D Kashchiev, WJ Lorenz, E Budevski. Surf. Sci. 82:364, 1979.

[41] S Manne, PK Hansma, J Massie, VB Elings, AA Gewirth. Science 251:183, 1991.

[42] (a) OM Magnussen, J Hotlos, RJ Nichols, DM Kolb, RJ Behm. Phys. Rev. Lett. 64:2929, 1990. (b) OM Magnussen, J Hotlos, G Beitel, DM Kolb, RJ Behm. J. Vac. Sci Technol. B 9:969, 1991. (c) K Sashikata, N Furuya, K Itaya. J. Electroanal. Chem. 316:275, 1991. (d) W Haiss, D Lackey, JK Sass, H Meyer, RJ Nichols. Chem. Phys. Lett. 200:343, 1992.

[43] FA Moller, OM Magnussen, RJ Behm. Phys. rev. B 51:2484, 1995.

[44] F Moller, OM Magnussen, RJ Behm. Electrochimica Acta 40:1259, 1995. J. Phys. Chem. 100:14721, 1996.

[45] MF Toney, JN Howard, J Richer, GL Borges, JG Gordon, OR Melroy, D Yee, LB Sorensen. Phys. Rev. Lett. 75:4472, 1995.

[46] (a) IM Tidswell, CA Lucas, NM Marković, PN Ross. Phys. Rev. B 51:10205, 1995. (b) CA Lucas, NM Marković, IM Tidswell, PN Ross. Physica B 221:245, 1996. (c) CA Lucas, NM Marković, PN Ross. Phys. Rev. B 56:3651-3654, 1997.

[47] (a) JX Wang, GM Waston, BM Ocko. J. Phys. Chem. 100:6672, 1996. (b) X Gao, GJ Edens, M Weaver. J. Phys. Chem. 98:8074, 1994.

[48] RR Adžić, JX Wang. J. Phys. Chem. in press, 1998.

[49] JX Wang, IK Robinson, RR Adžić. Surf. Sci. in press, 1998.

FIGURES

FIG. 1. Schematic illustrations of a (2×2) monolayer at a single crystal surface (a), and the corresponding 3D (b) and 2D (c) diffraction patterns. The solid and dashed lines in (b), and the filled and open circles in (c) represent the crystal truncation and surface rods, respectively. Typical crystal truncation rod (solid line) and monolayer surface rod (dashed line) profiles are shown in (d).

FIG. 2. Cross-section of thin layer x-ray electrochemical cell.

FIG. 3. Linear sweep voltammograms obtained at 2 mV/s for the UPD of Bi on the gold surfaces in 0.1 M $HClO_4$ containing 2.5 mM Bi_2O_3. Dashed line shows the onset of bulk deposition. Insert: Atomic model of the close-packed Bi monolayer on Au(111).

FIG. 4. Observed in-plane diffraction patterns (left) and corresponding real space models (right) for Bi monolayers on the Au(100) and Au(110) surfaces at potentials close to the onset of bulk deposition. The relative size of Bi and Au atoms in their bulk solids are represented by the size of the filled and open circles.

FIG. 5. Layer density of the Tl (> -0.4 V), Pb (> -0.18 V), and Bi (> 0.25 V) monolayers on the low index gold surfaces as a function of potential. The diameters given for Tl and Pb are the nearest neighbor separations within the hexagonal layers in the bulk crystals [27]. For Bi, the "equivalent bulk diameter" is calculated from the rhombohedral bulk crystal [27] by assuming a fcc structure with the same unit cell volume. The layer density is calculated from the hexagonal unit cell area with the bulk diameter as the lattice constant divided by the unit cell area measured for the monolayer.

FIG. 6. (top) Models of the $c(\sqrt{2}\times 2\sqrt{2})R45°$ and $c(2\times 2)$ Br adlayers on Au(100) and Ag(100), respectively. (bottom) In-plane diffraction patterns for the above models.

FIG. 7. Linear sweep voltammogram from Au(100) in 0.05 M NaBr. Sweep rate 10 mV/s.

FIG. 8. 1D commensurate-incommensurate phase transition in electrosorption of Br on Au(100). Inserts: Atomic models of the Br adlayer at potentials below and above the critical point of the phase transition.

FIG. 9. Results for the electrosorption of bromide on the Ag(100) surface. The scattered intensities, after background subtraction, are shown at (1/2,1/2) and (0,1) versus the applied potential. The corresponding cyclic voltammogram curve (10 mV/s) is shown in the lower panel.

FIG. 10. (top) Voltammetry curve for the UPD of Tl on Au(111) in 0.1 M $HClO_4$ containing 1 mM TlBr. Sweep rate 20 mV/s. (bottom) Potential dependent diffraction during the negative (solid line) and positive (dashed line) potential scans (0.5 mV/s) at (9/13,3/13), (2/3,1/6), and (0.468,0.468) positions for the $(\sqrt{13} \times \sqrt{13})$, $(3 \times \sqrt{3})$, and $c(2.14 \times \sqrt{3})$ phases, respectively. Coverages, in units of monolayers of the Au substrate, shown by the open and filled circles for Br and Tl, respectively, are calculated from the adlayer lattice constants.

FIG. 11. (a) and (b) Structural models where the Au(111) surface atoms (2.885 Å), Tl ions (2.98 Å), and anions (Br 3.92 Å, I 4.30 Å) are respectively represented by the open, light shade, and heavy shade circles. (c) and (d) Observed in-plane diffraction pattern from the $(\sqrt{13} \times \sqrt{13})$ and (3×3) phases, respectively. The sizes (area) of the open circles are proportional to the measured structure factor intensities and the sizes of the "+" sign are proportional to the calculated values based on the models shown above.

FIG. 12. Specular reflectivity profile obtained from the TlI_3-(3×3) adlayer on Au(111).

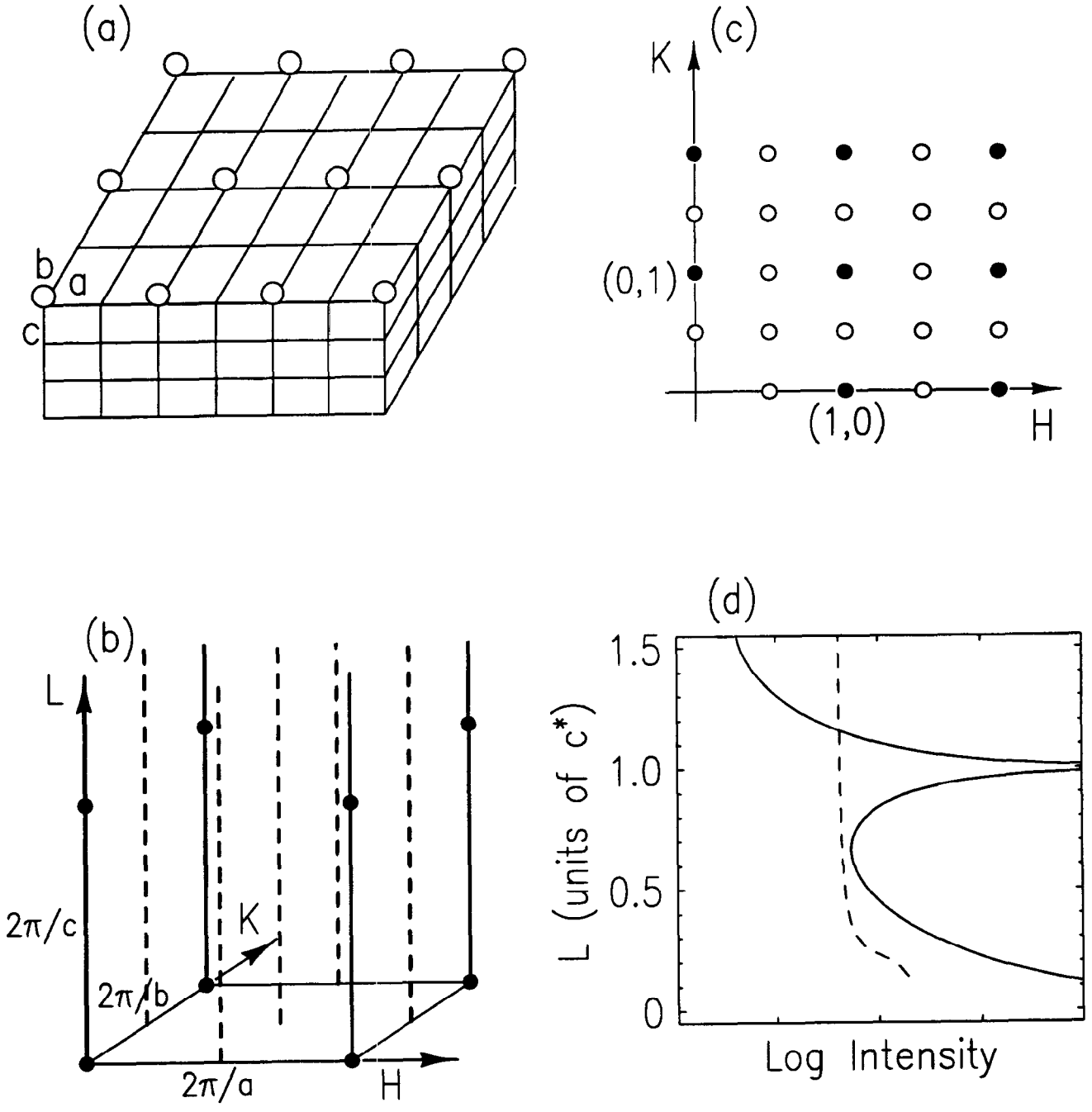
(a)
b
a
c
(c)
K
(0,1)
(1,0)
H
(b)
L
2π/c
K
2π/b
2π/a
H
(d)
1.5
1.0
0.5
0
L (units of c*)
Log Intensity

Fig. 1

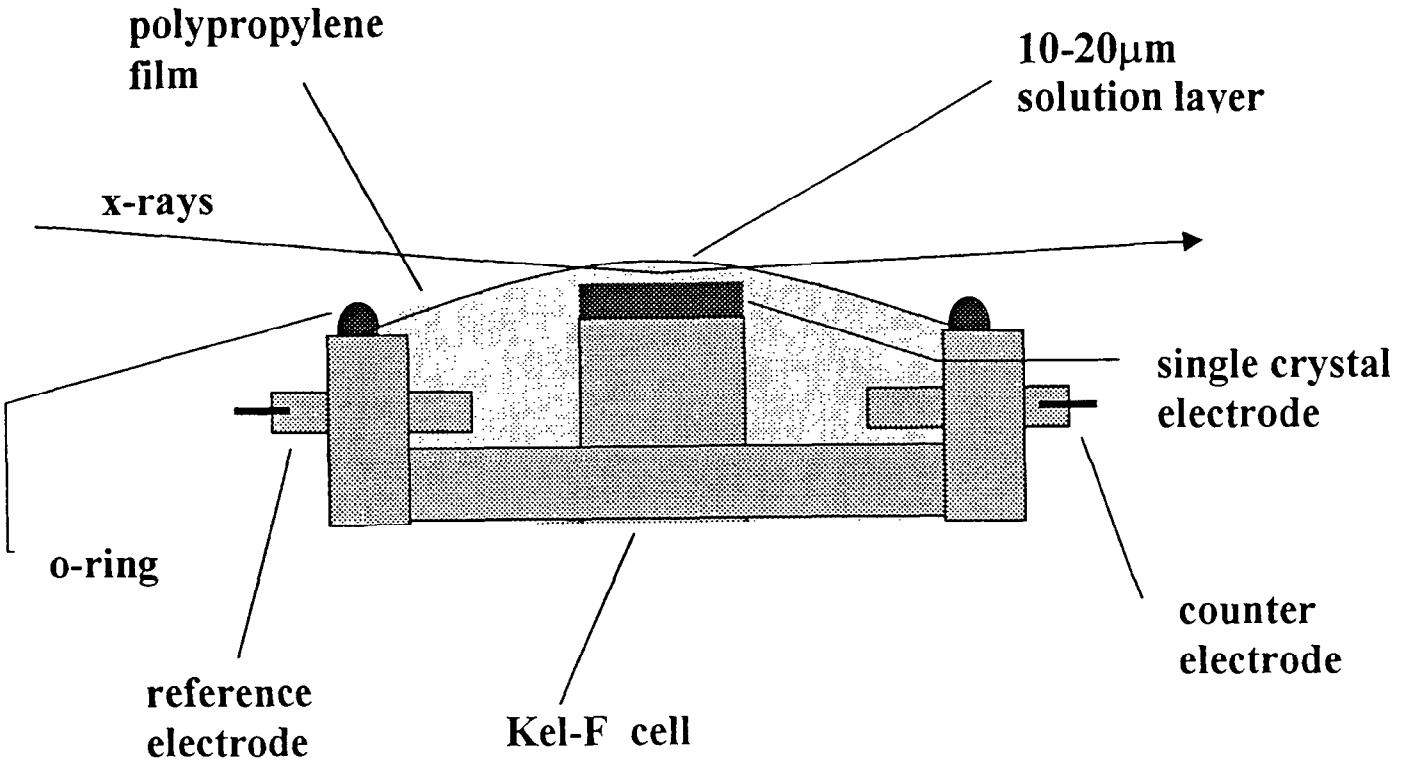
polypropylene
film
10-20μm
solution layer
x-rays
single crystal
electrode
o-ring
counter
electrode
reference
electrode
Kel-F cell

Fig. 2

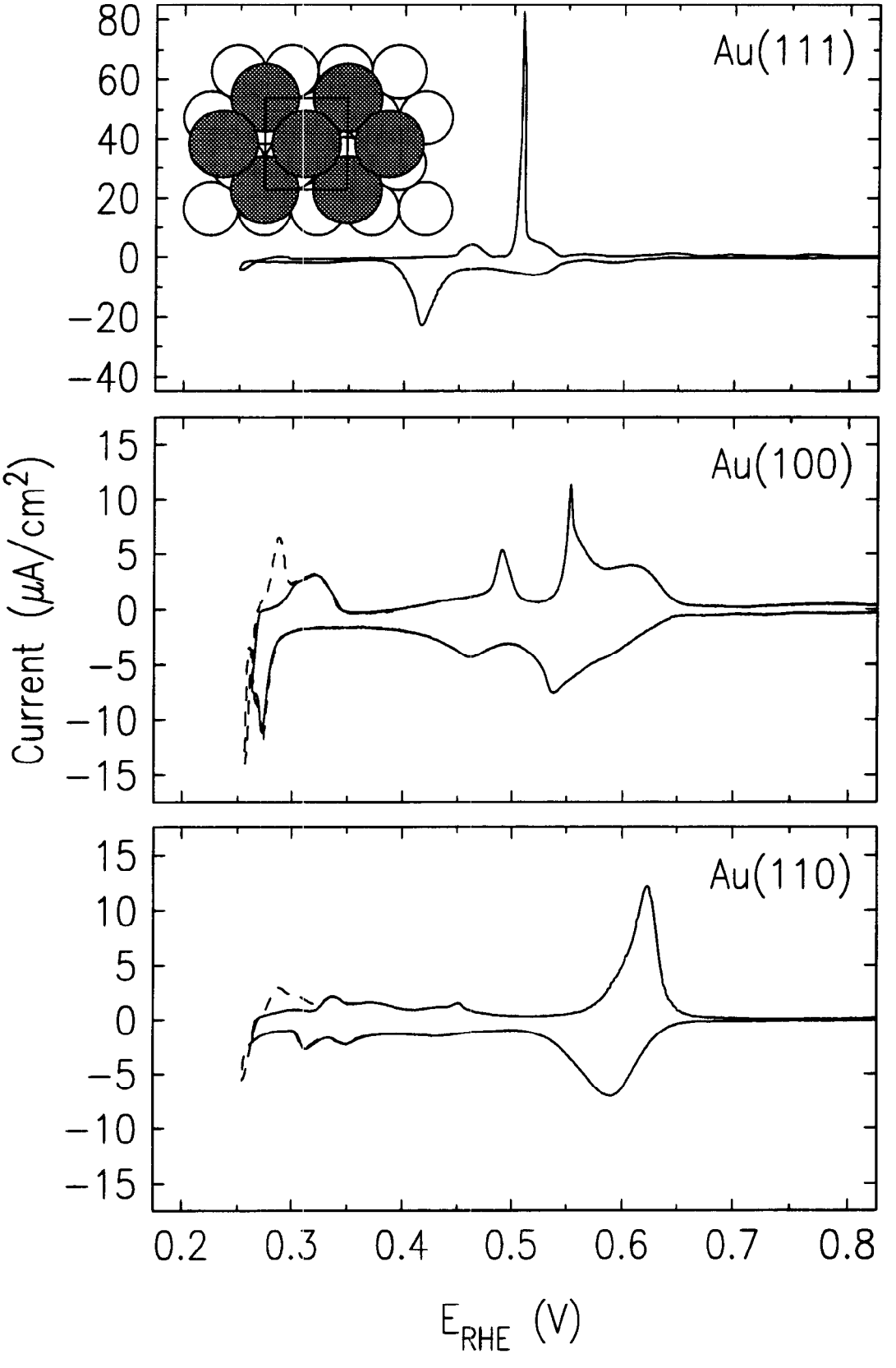
Au(111)
Au(100)
Au(110)
80
60
40
20
0
−20
−40
15
10
5
0
−5
−10
−15
Current (μA/cm²)
0.2
0.3
0.4
0.5
0.6
0.7
0.8
E_RHE (V)

Fig. 3

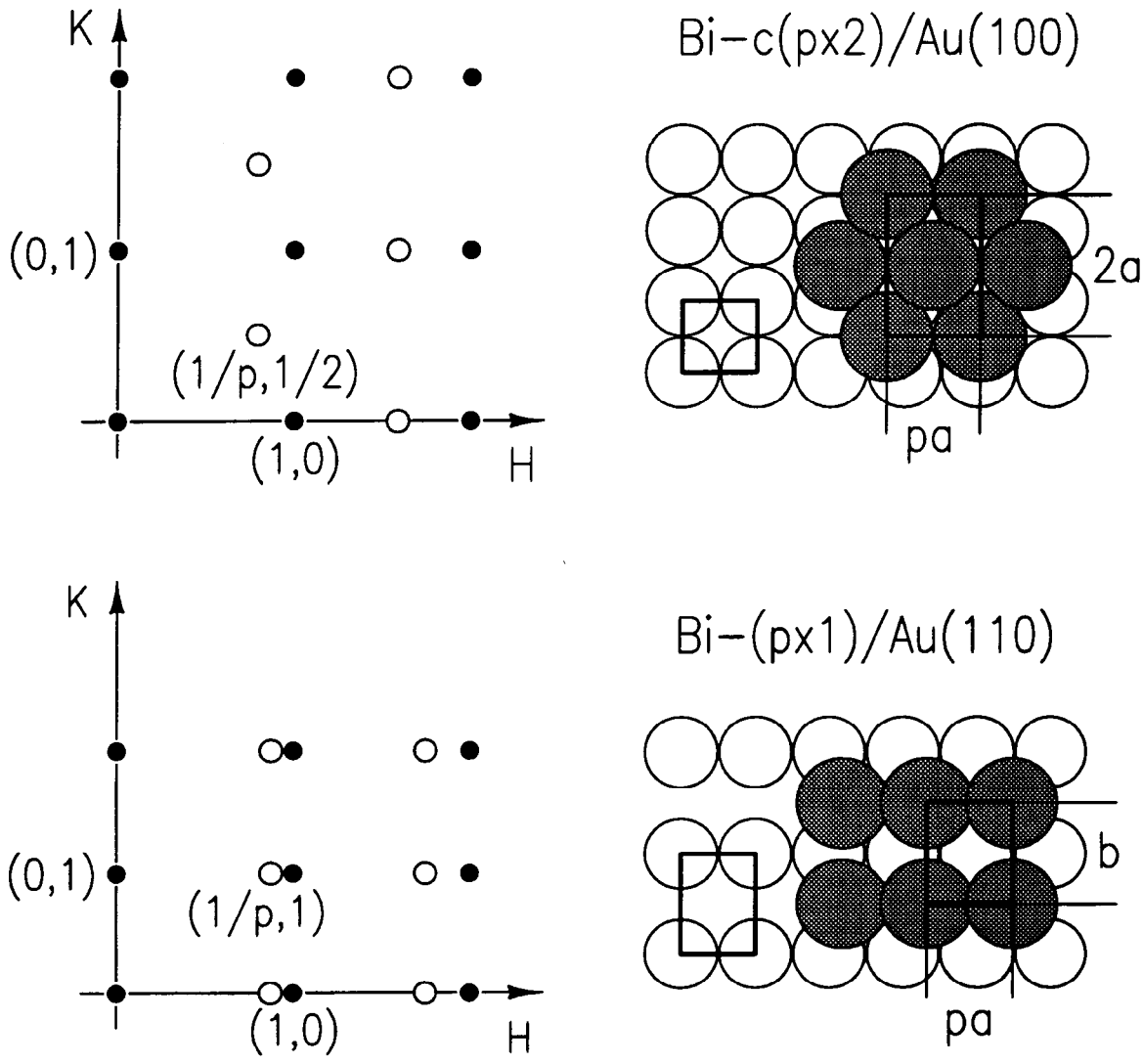

Fig. 4

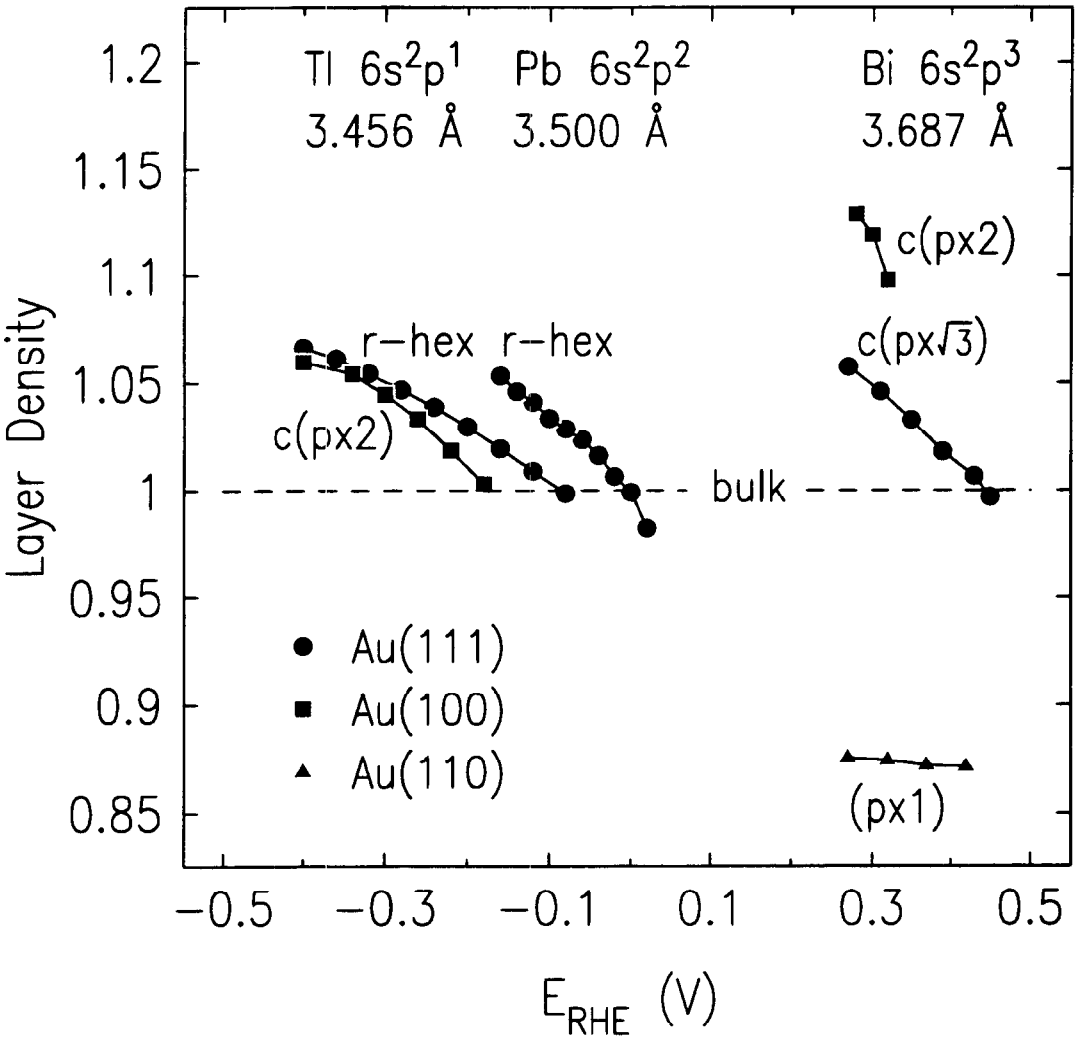
Tl 6s²p¹ Pb 6s²p²
3.456 Å 3.500 Å
Bi 6s²p³
3.687 Å
c(px2)
r–hex r–hex
c(px√3)
c(px2)
bulk
Au(111)
Au(100)
Au(110)
(px1)
Layer Density
1.2
1.15
1.1
1.05
1
0.95
0.9
0.85
−0.5 −0.3 −0.1 0.1 0.3 0.5
E_RHE (V)

Fig. 5

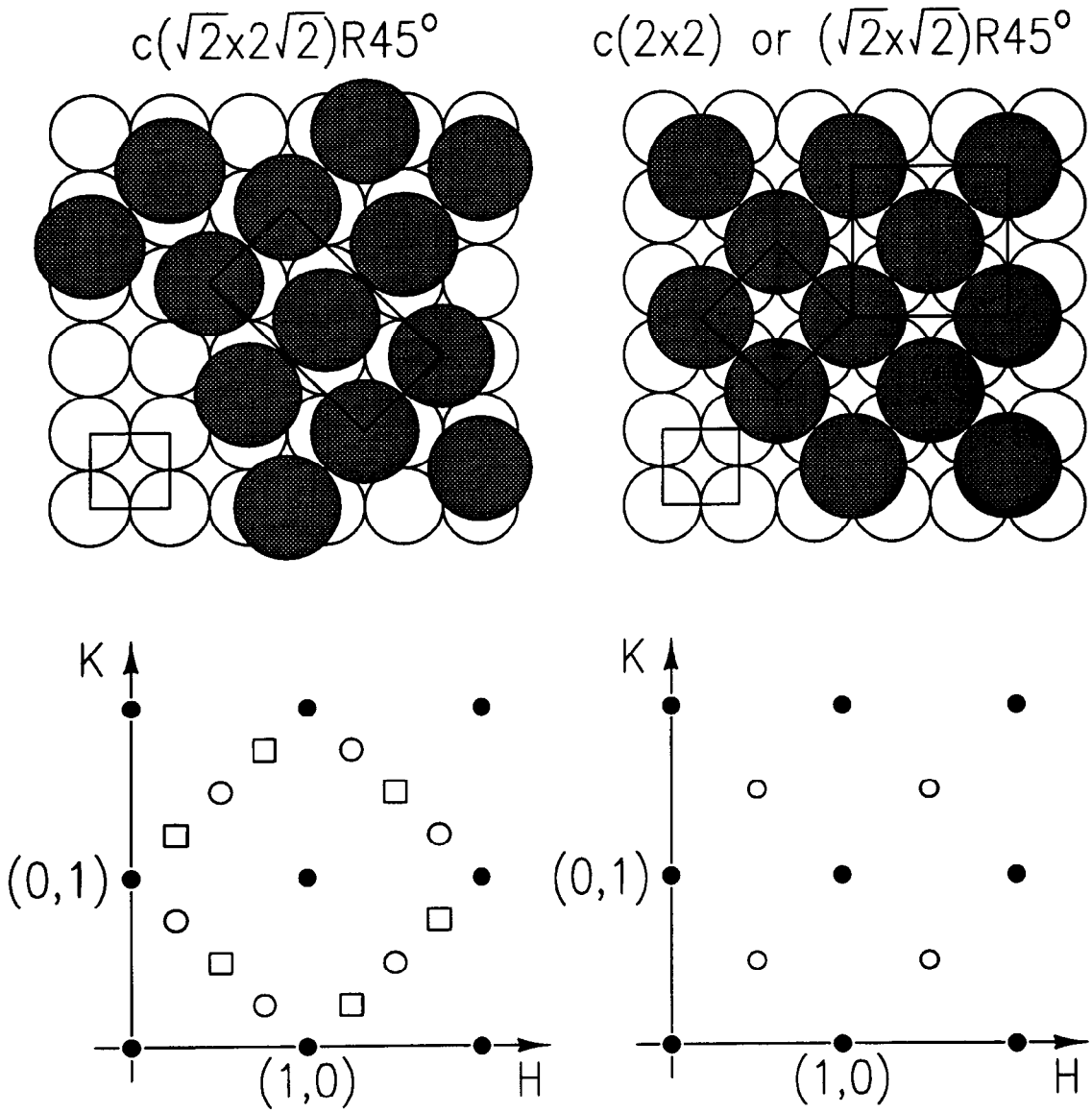

Fig. 6

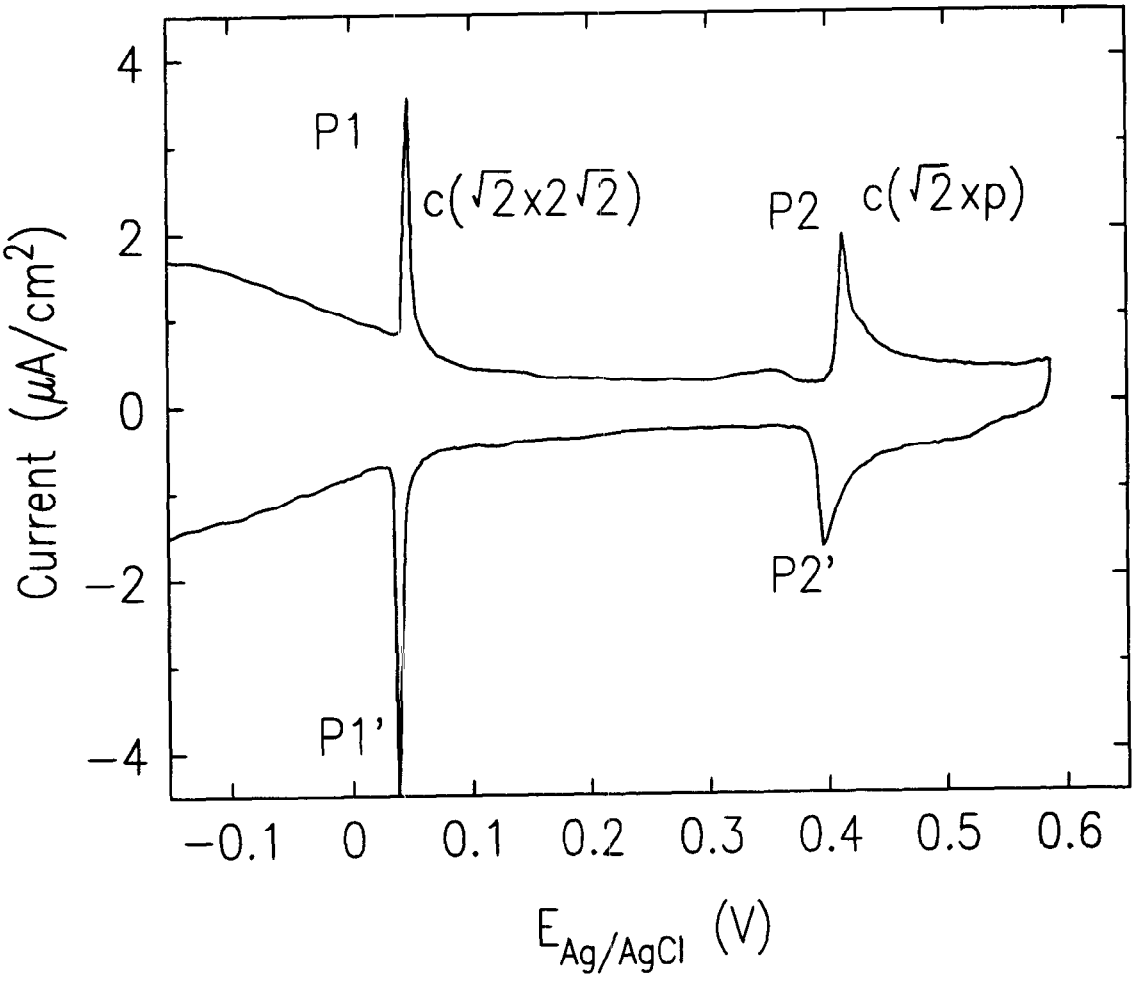
4
2
0
−2
−4
P1
c(√2x2√2)
P2
c(√2xp)
P2'
P1'
−0.1
0
0.1
0.2
0.3
0.4
0.5
0.6
Current (μA/cm²)
E Ag/AgCl (V)

Fig. 7

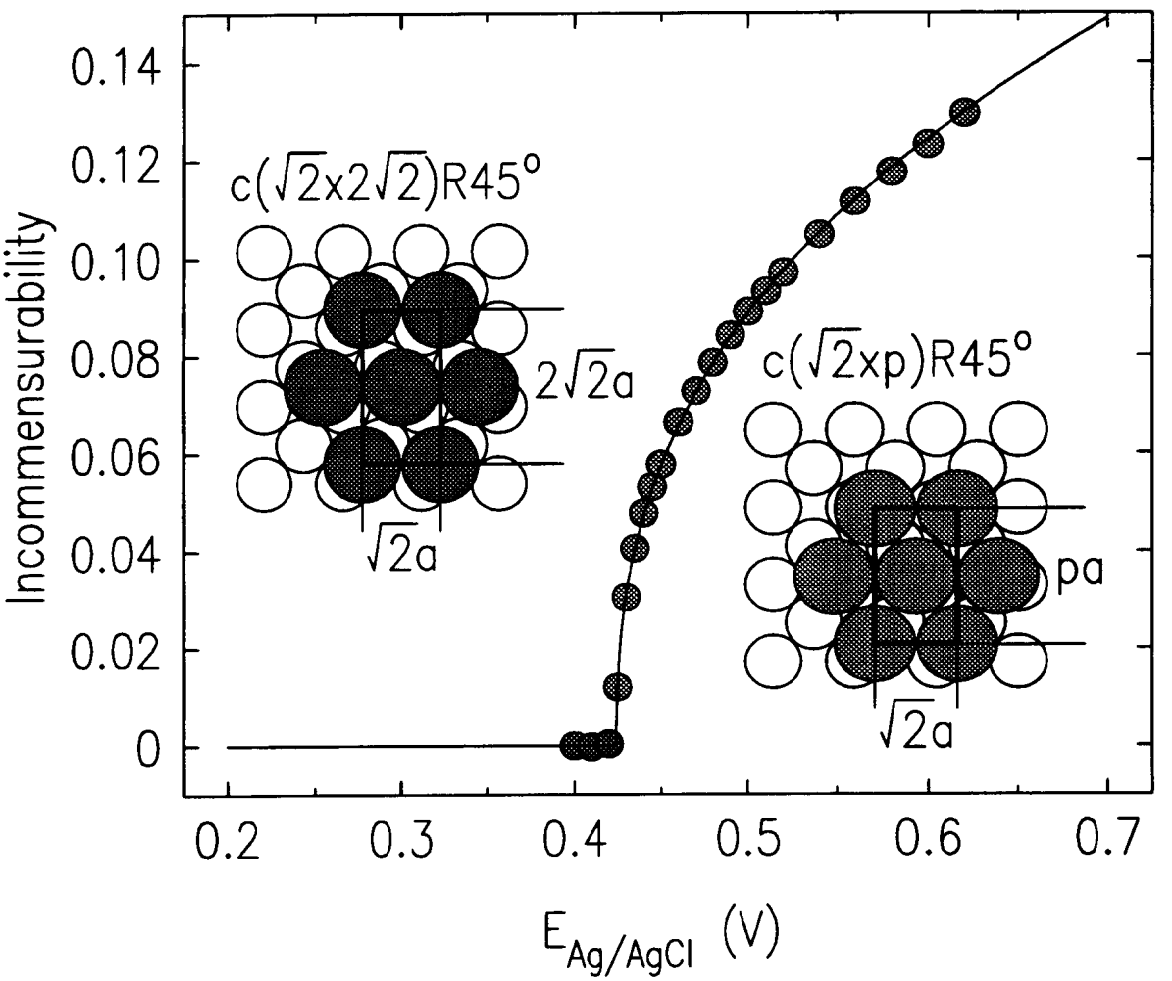
Incommensurability
0.14
0.12
0.10
0.08
0.06
0.04
0.02
0
0.2
0.3
0.4
0.5
0.6
0.7
$E_{Ag/AgCl}$ (V)
c(√2x2√2)R45°
2√2a
√2a
c(√2xp)R45°
pa
√2a

Fig. 8

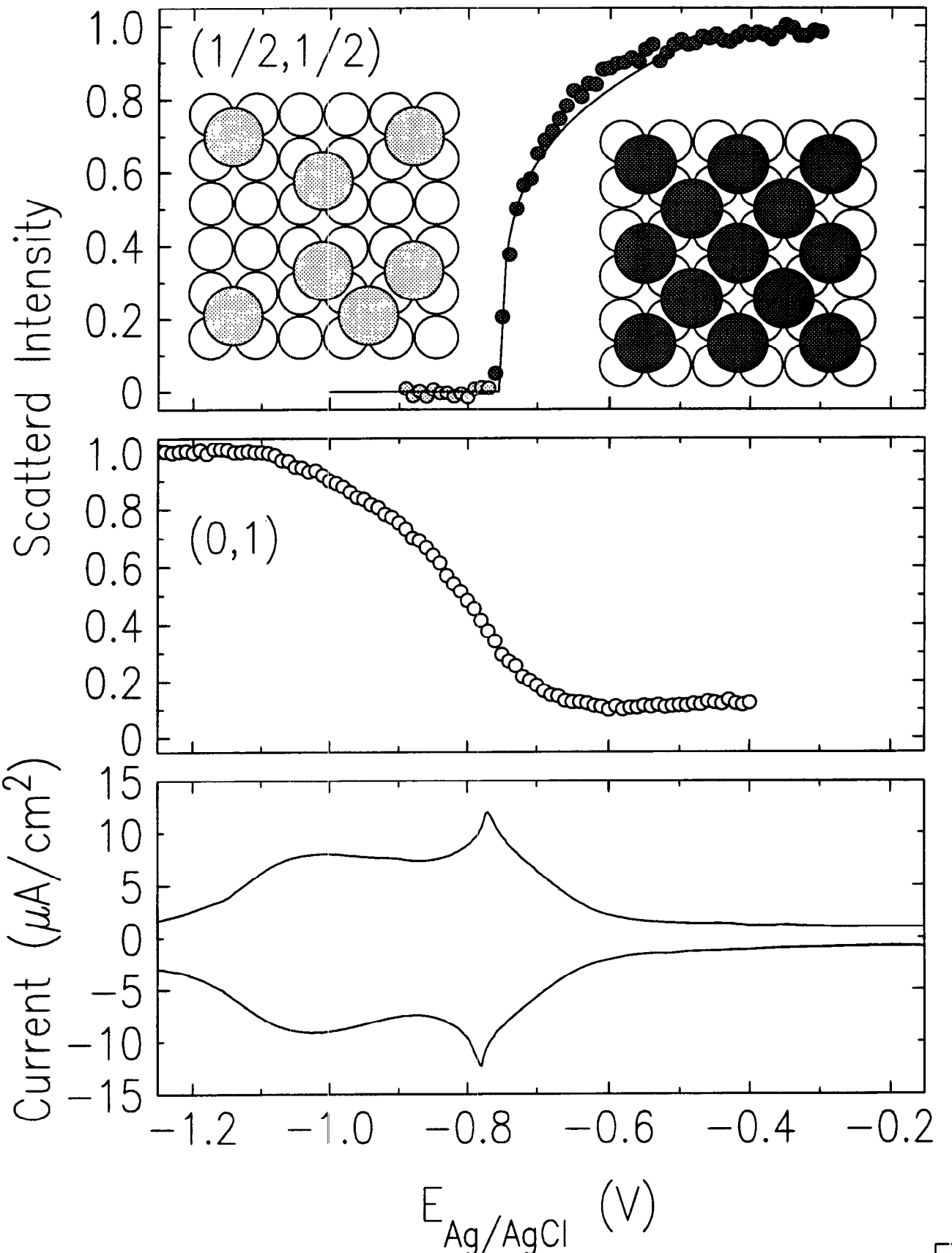
(1/2,1/2)
(0,1)
Scatterd Intensity
Current (μA/cm²)
E Ag/AgCl (V)
1.0
0.8
0.6
0.4
0.2
0
15
10
5
0
−5
−10
−15
−1.2
−1.0
−0.8
−0.6
−0.4
−0.2

Fig. 9

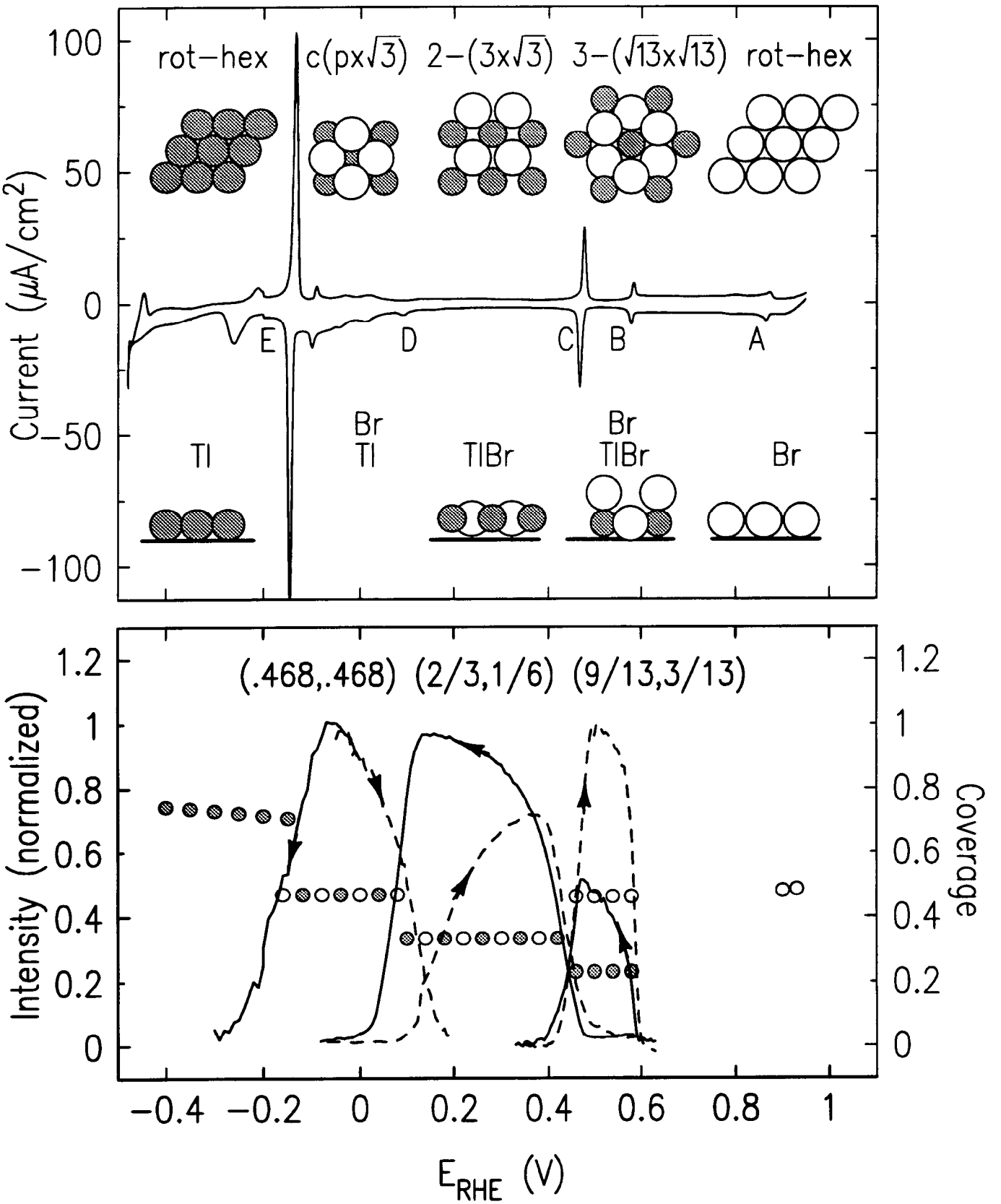
rot–hex
c(px√3)
2–(3x√3)
3–(√13x√13)
rot–hex
100
50
0
−50
−100
Current (μA/cm²)
E
D
C
B
A
Tl
Br
Tl
TlBr
Br
TlBr
Br
(.468,.468)
(2/3,1/6)
(9/13,3/13)
1.2
1
0.8
0.6
0.4
0.2
0
Intensity (normalized)
Coverage
∞
−0.4
−0.2
0
0.2
0.4
0.6
0.8
1
E_RHE (V)

Fig. 10

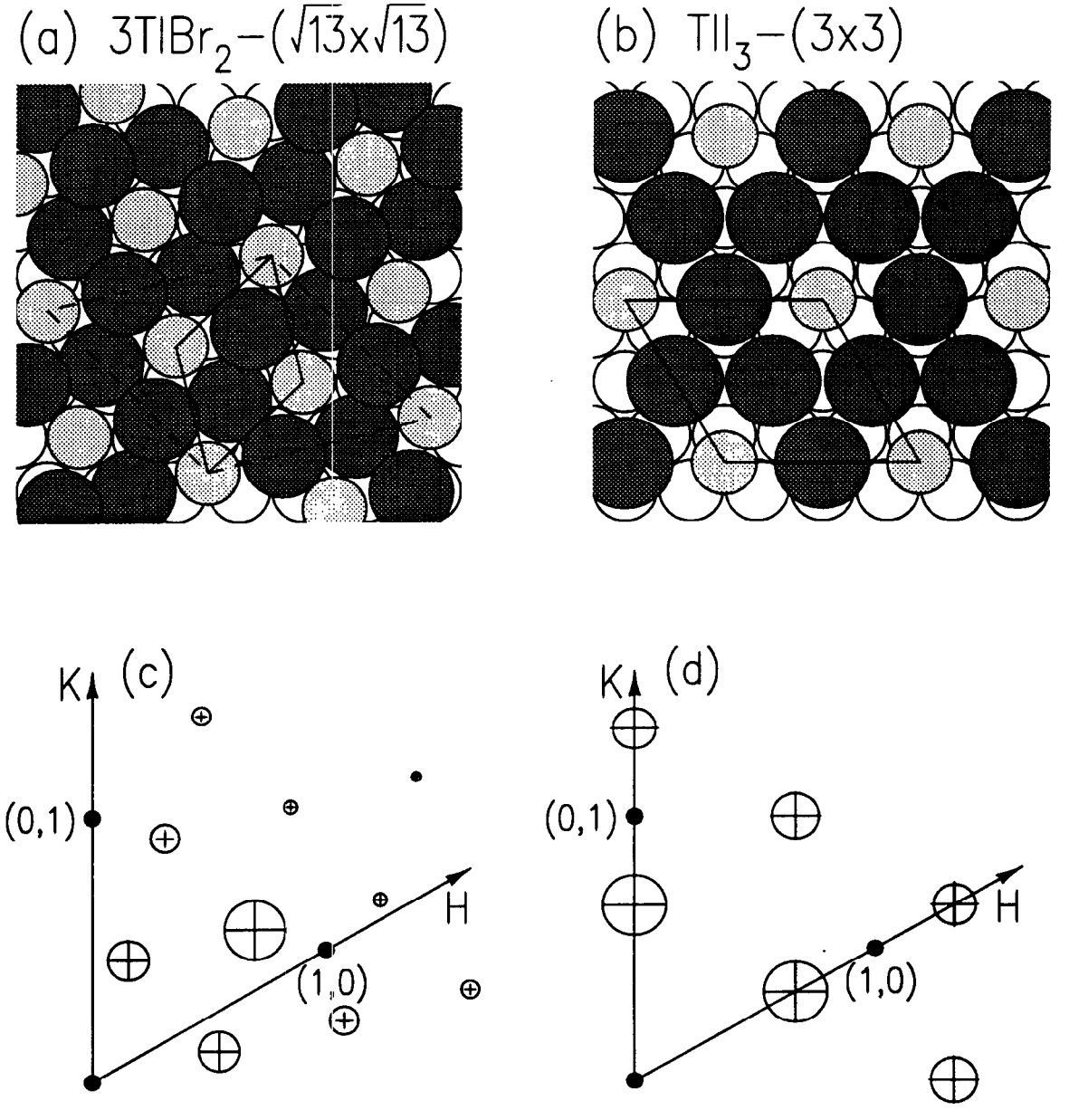

Fig. 11

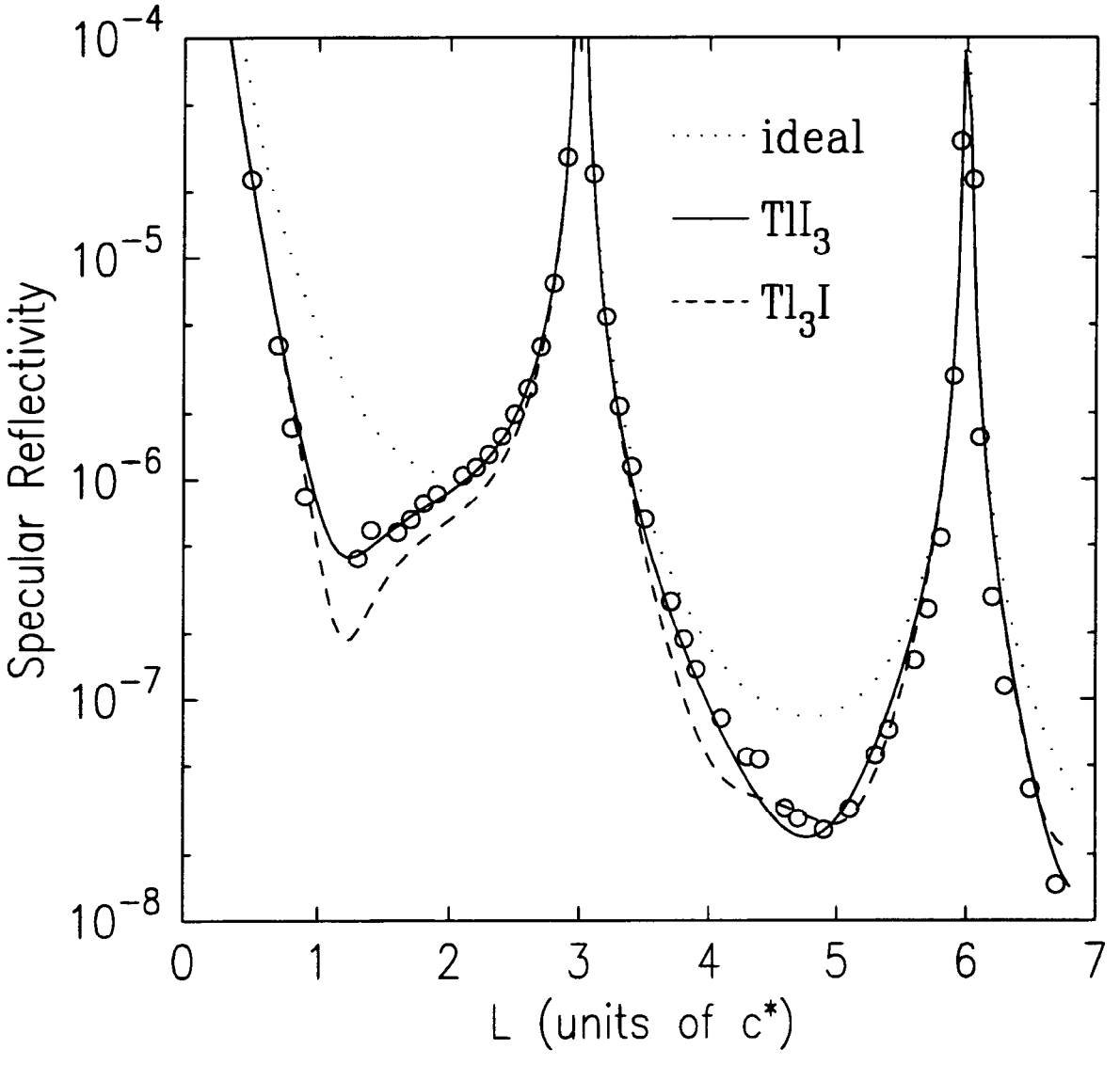
Specular Reflectivity
10^{-4}
10^{-5}
10^{-6}
10^{-7}
10^{-8}
0
1
2
3
4
5
6
7
L (units of c*)
ideal
TlI_3
Tl_3I

Fig. 12